Journal of Engineering Mathematics **50:** 289–309, 2004.

Thin-film flows near isolated humps and interior corners

O.E. JENSEN, G.P. CHINI[1] and J.R. KING
School of Mathematical Sciences, University of Nottingham, University Park, Nottingham NG7 2RD, U.K.; Author for correspondence: Oliver.Jensen@nottingham.ac.uk; [1]*Department of Mechanical Engineering, University of New Hampshire, Durham, NH 03824, U.S.A.*

Received 12 December 2003; accepted in revised form 12 July 2004

Abstract. This paper concerns the surface-tension-driven flow of a thin layer of viscous liquid following a sudden change in the shape of its substrate. It is assumed that the substrate either develops an isolated hump or bends to create an interior corner. The flow is modelled using an evolution equation derived from lubrication theory, extended in the case of a corner with fully nonlinear expressions for interfacial curvature and volume conservation. Numerical simulations and large-time asymptotics are used to describe the evolution of the film. Over long times the film typically forms a quasi-static puddle adjacent to the hump (or in the corner) and a wave-like disturbance propagates into the far field. For sufficiently large humps and sharp corners, the film pinches off to form an effective contact line at the edge of the puddle, at which the film height tends to zero as time tends to infinity; as long as the film does not rupture (which it cannot in the mathematical framework adopted), the effective contact line drifts slowly away from the hump towards a limiting position dictated by the transient dynamics. Flows off humps with maxima less than a critical height have a qualitatively different structure, captured by one of two possible branches of similarity solutions of the thin-film equation, whereby pinch-off does not occur.

Key words: lubrication theory, self-similarity, surface tension, thin-film flow

1. Introduction

This paper is concerned with the surface-tension-driven readjustment of a thin layer of viscous liquid following a sudden change in the shape of adjacent solid surfaces. Typical situations that we envisage are illustrated in Figure 1 (a–c). An initially uniform liquid layer coating a flat plane may be disturbed either though a sudden change in the shape of its substrate (for example the formation of a localised hump, or bending of the substrate to form an interior corner), or through sudden contact between the liquid layer and a second surface, which itself may be wet or dry (for example a sphere that is brought into contact with a film coating a flat plane). Such situations arise widely in industrial contexts, for example when geometrical imperfections or external disturbances create defects in coatings. Important biological applications arise in the lung, when the liquid lining of an airway redistributes following the impact of an inhaled particle, or following contact between the wet walls of a collapsing airway [1]; similar flows arise in the eye [2], where the tear film coats the curved cornea. In the flows we consider here the film typically evolves to form a quasi-static puddle connected to a liquid film of unbounded lateral extent (Figure 1d). The capillary pressure in the puddle (the free surface of which has negative curvature) is lower than that in the far field, where the uniform film sits on a flat substrate. The resulting pressure gradient pulls fluid into the puddle, allowing the puddle to grow indefinitely (or until the films thins sufficiently for intermolecular forces to become significant, for example causing the film to rupture). We wish to determine the rate at

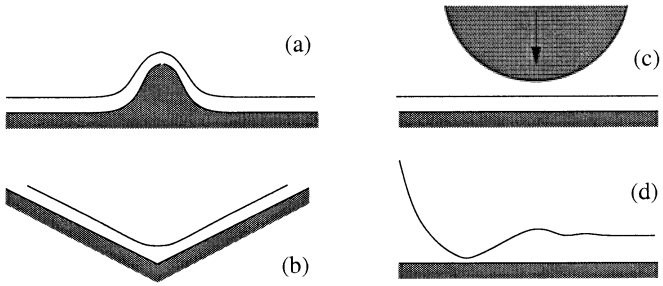

Figure 1. Typical thin-film flows relevant to the present study: (a) a film coating a hump; (b) a film in an interior corner; (c) a film between touching surfaces. A common feature is a puddle connected to an unsteady capillary wave (d).

which the puddle grows and its volume at large times. Such considerations are significant for example when evaluating the adhesive capillary force between touching wet surfaces.

The redistribution of the liquid film is driven by surface tension, mediated by gradients in the curvature of the substrate. These gradients may either be spatially distributed (in the case of a hump) or concentrated near a point (in the case of a corner). A number of models have been proposed to describe thin-film flows on non-uniformly curved surfaces, most taking the classical thin-film equation of lubrication theory [3, 4] as a starting point. Schwartz and Weidner [5], for example, included a driving curvature-gradient term in the thin-film equation to model flow off an exterior corner in a bounded domain. While their model gives realistic predictions, it is not strictly asymptotically consistent (in the problem they studied) because the driving curvature gradient varied on a lengthscale short compared to the film depth (moreover, such formulations in body-fitted coordinates may not conserve mass accurately [6]). Others have used a similar formulation to describe levelling flows on non-uniform surfaces [7] and flows driven by a pressure gradient or body force over non-uniform topography [8, 9]. The classical lubrication-theory approach is uniformly valid in space when gradients in the curvature of the substrate and of the interface vary on lengthscales that are long compared to the film depth. In this limit, lubrication theory has been used to model the readjustment of a thin liquid layer in a weakly curved cylindrical tube [10] and off a hump in a bounded domain [11, 12].

Asymptotically rational models for flows over arbitrarily curved surfaces, subject to various constraints on the substrate curvature gradient and film thickness, have been derived by a number of authors [6, 13, 14]. The resulting evolution equations differ in specific details, but between them account for corrections ensuring mass conservation when employing body-fitted coordinates [6], weakly nonlinear corrections to the expression for interfacial curvature, a geometric correction to the mobility term in the expression for the flux [6], and three-dimensional effects [6, 13, 14]. An alternative approach to such problems is to formulate an evolution equation that is effectively a composite asymptotic approximation in which the classical thin-film equation is extended by retention of exact curvature terms in the expression for the pressure gradient, and by incorporation of geometrical factors ensuring exact mass conservation in body-fitted coordinates [11, 15]. This strongly nonlinear but partially *ad hoc* approach provides an accurate description both of regions of the flow in which the film is relatively deep and quasi-static, and in which the film is thin and unsteady. Provided the thin film is formed exclusively of such regions, this approach has been shown to compare well to full Stokes-flow computations in a specific problem related to lung airways [15]. Of course, such an approach is unlikely to provide an accurate description of regions of the flow where

a deep film evolves unsteadily, and so for example may not provide an approximation that is uniformly valid in time. A similar strategy has been followed by Stocker and Hosoi [16, 17], who used a hyperbolic coordinate system to derive evolution equations for thin-film flows in 90° corners.

The problems studied below address a simple issue. In configurations in which a film evolves to a configuration in which a quasi-static puddle is connected to a spatially unbounded film (Figure 1d), a pressure gradient will continually drive fluid into the puddle, causing it to grow. We wish primarily to establish the dynamics of the effective contact line at the edge of the puddle and of the overall film. Howell [13] studied a related problem, when the curvature gradient at an interior corner is distributed over a long lengthscale so that the film's evolution can be described by a hyperbolic equation, in which the film dynamics are driven entirely by substrate gradients. Aradian, Raphaël and de Gennes [18] examined the structure of the margins of a soap film, showing how a self-similar capillary wave is connected to a static border through a thin draining region of the kind described by Jones and Wilson [19]. We present numerical simulations revealing how a similar asymptotic structure arises for flows driven off sufficiently tall humps or sharp corners. A detailed asymptotic analysis reveals new spatial and temporal behaviour explaining how fluid volume is distributed during the flow's evolution. We then show how a qualitatively different flow structure arises for shallow humps, associated with one of two possible branches of similarity solutions of the thin-film equation.

The paper is organised as follows. In Section 2 we describe the formulation of our model for thin-film flow off humps (using classical lubrication theory) and in interior corners (using a composite evolution equation, parameterized using a method of spines following [15]). Numerical results (Section 3) are then used to motivate and validate large-time asymptotic approximations (Section 4).

2. Models and methods

We briefly describe the evolution equations governing flow off a hump (2) and in a corner (7) before outlining our numerical method (Section 2.2).

2.1. Problem formulation

We model the flow of a two-dimensional incompressible Newtonian fluid of constant viscosity μ bounded above by a passive gas and below by a rigid, possibly curved, stationary substrate. We assume that the surface tension σ acting at the free surface is uniform and we neglect gravity and van der Waals forces. For low-Reynolds-number thin-film flows above a flat substrate, classical lubrication theory [4] yields the well-known evolution equation

$$h_t + \frac{1}{3}(h^3 h_{xxx})_x = 0 \tag{1}$$

for $h(x, t)$, the non-dimensional height of the film measured normal to the substrate. Here subscripts denote partial derivatives with respect to distance along the flat substrate x and time t. In (1), h is scaled on H_∞, the undisturbed far-field film thickness, while x is scaled on H_∞/ε for some $\varepsilon \ll 1$ and t on $\mu H_\infty/\varepsilon^4\sigma$. Consistent with the lubrication approximation, the non-dimensional pressure $p = -h_{xx}$, where p is scaled on $\varepsilon^2\sigma/H_\infty$.

2.1.1. *Hump*

When gradients in substrate curvature vary over distances large compared to the fluid depth, they can be incorporated into (1) in an asymptotically consistent fashion, yielding [5]

$$h_t + \frac{1}{3}(h^3(h+g)_{xxx})_x = 0, \tag{2}$$

where the substrate and free-surface locations lie at $y = g(x)$ and $y = g(x) + h(x,t)$, respectively, in Cartesian (x, y)-coordinates. We employ (2) to model capillary-driven flow off of a Gaussian-shaped hump by setting

$$g(x) = g_0 \exp[-(x/2d)^2]. \tag{3}$$

The $O(1)$ parameters g_0 and d are specified below. Here we may regard ε as the ratio of H_∞ to the dimensional hump width. We shall examine solutions of (2) on a finite domain $0 \le x \le L$, where $L \gg 1$ is sufficiently large for the film to remain undisturbed near $x = L$ over the times of interest. We impose a uniform initial condition $h(x,0) = 1$ for $0 < x < L$ and symmetry and zero-flux boundary conditions,

$$h_x(0,t) = h_{xxx}(0,t) = h_x(L,t) = h_{xxx}(L,t) = 0. \tag{4}$$

2.1.2. *Interior corner*

The hump formulation above is firmly based in rational thin-film asymptotics. However, although several authors have derived evolution equations for flows over curved substrates [6, 13, 14], none of these equations remains asymptotically consistent in the limit when gradients in substrate curvature vary over a lengthscale short compared to the film depth; in particular, none can rationally describe flow near a sharp interior (or exterior) corner, where the substrate curvature is singular.

It is natural to attempt a formulation in which the domain of interest excludes the corner, its presence being imposed instead via specification of appropriate boundary conditions. We briefly describe this approach and its pitfalls before outlining a method that we have found more satisfactory. As shown in Figure 2, we let the y-axis bisect a corner of interior semi-angle α and intersect the free surface at some point. The time-varying distance (measured along the substrate) between the corner and the normal projection of this point onto one of the walls is denoted by $s_u(t)$. If s measures distance along that wall from $s_u(t)$, then, for $s > 0$, the substrate is flat and the location of the free surface can be uniquely specified by measuring the film height $h(s,t)$ normal to the substrate. In this formulation, (1) becomes

$$h_t - \dot{s}_u h_s + \frac{1}{3}(h^3 h_{sss})_s = 0, \tag{5}$$

where $\dot{s}_u \equiv \mathrm{d}s_u/\mathrm{d}t$ must be determined by enforcing the geometric constraint $h(0,t) = s_u \tan\alpha$. Boundary conditions at $s = 0$ arise from imposition of zero mass flux across the corner bisector (for flows symmetric with respect to the bisector) and symmetry about the y axis; the latter condition requires $h_s(0,t) = -\cot\alpha$.

A necessary condition for (5) to be asymptotically consistent is for $\gamma \equiv \pi/2 - \alpha \to 0^+$ (*i.e.*, for very shallow corners), for only then is $|h_s(s,t)|$ assured to be uniformly small. In that limit, the initial boundary-value problem simplifies to (1), subject to

$$h_x(0,t) = -\gamma/\varepsilon, \quad h_{xxx}(0,t) = 0, \quad h_x(L,t) = 0, \quad h_{xxx}(L,t) = 0, \tag{6}$$

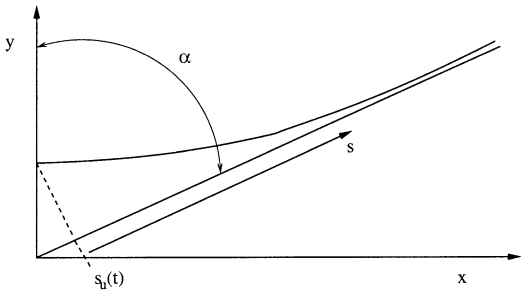

Figure 2. Corner geometry. The computational domain is $s \geq 0$.

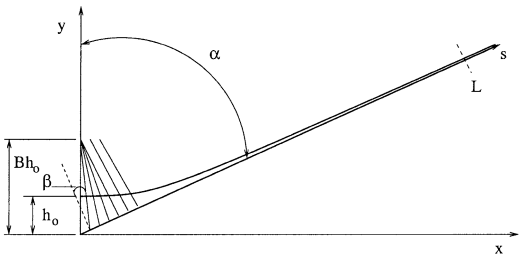

Figure 3. Computational domain for simulations of draining into an interior corner. $\beta(s)$ measures the angle between the spine and substrate normal. h_0 is the initial height of the corner puddle.

i.e., $s \approx x$ and $s_u(t) \approx 0$. Unfortunately, this formulation proves to be numerically ill-conditioned, exhibiting large volume fluxes near $x = 0$. The source of the difficulty – and the means for its amelioration – may be understood by recalling that the corner represents a discontinuity in substrate curvature; indeed, setting $g_{xx}(x) = 2(\gamma/\varepsilon)\delta(x)$ where $\delta(x)$ is the Dirac delta function, the problem is formally equivalent to (2) subject to (6) with $h_x(0, t) = 0$ replacing the inhomogeneous slope condition. Analysis of the solution as $x \to 0$ indicates that $h_{xxx} \sim 2(\gamma/\varepsilon)\mathrm{d}\delta/\mathrm{d}x$, accounting for the singular fluxes near the origin observed in simulations. This formulation may be regularised via appropriate smoothing of $g_{xx}(x)$.

Although (5) is not consistent for sharp corners when γ is $O(1)$, the singularity in substrate curvature does not directly pose numerical difficulties, since, for sufficiently deep corner puddles, the computational domain does not border the corner, *i.e.*, $s_u(t)$ is bounded away from zero. To improve the accuracy of (5) in regions where $|h_s(s, t)|$ is not small, $h_{ss}(s, t)$ can be replaced with $k(s, t)$, the exact curvature of the interface (see (11) below). Nevertheless, there remains an inherent difficulty with this approach related to the specification of $q(0, t)$, the flux across $s_u(t)$. This flux is determined by enforcing global volume conservation, where the total fluid volume is

$$V = \frac{s_u^2}{2}\tan\alpha + \int_{s_u(t)}^{L} h(S, t)\mathrm{d}S.$$

Setting $\mathrm{d}V/\mathrm{d}t = 0$, using Leibnitz's rule and substituting $h_t = -q_S$, where $S \equiv s + s_u(t)$, we find $q(0, t) = 0$. Given the zero-flux condition across the corner bisector, this implies that $\dot{s}_u = 0$ – a contradiction unless the puddle height remains fixed. (Numerical simulations based on this formulation show time-dependent puddle heights and, thus, cannot conserve mass accurately in body-fitted coordinates.)

There are therefore a number of difficulties in extending classical lubrication theory to describe flows near an interior corner. We have therefore employed an alternative formulation, namely Heil and White's [15] modified thin-film equation coupled to a parameterization of the film thickness using spines. The composite evolution equation

$$\rho_t + \frac{1}{3}(h^3 k_s)_s = 0 \tag{7}$$

provides an accurate description of flows in which a deep quasi-static puddle is connected to a thin film, since it (a) conserves mass in appropriate coordinates, (b) enforces the exact Young-

Laplace constraint in regions where the film is deep and (c) accurately predicts the unsteady dynamics of thin-film regions and, hence, the fluid flux into (or out of) the corner puddle. As shown in Figure 3, s in (7) measures distance along the flat substrate from the corner, while h measures the height of the film along certain prescribed directions (spines) [20]. We set the spine-angle distribution

$$\beta(s) = \left[\frac{1-\tanh((s-s_*)/\Delta)}{2}\right]\left[\tan^{-1}\left(\frac{Bh_0 - s\ \cos\ \alpha}{s\ \sin\ \alpha}\right) - \alpha\right], \tag{8}$$

where h_0 is the initial height of the corner puddle, the spine-distribution parameters Δ and B are given below and $s_* = Bh_0[\sin\,\alpha(\cot\,\alpha + \tan\,\alpha)]^{-1}$. By selecting B appropriately, the spines do not intersect within the interior of the fluid (near $s = 0$, they intersect the y-axis at a height B times the initial puddle height), and they become normal to the substrate at $s \approx s_*$, before the film becomes thin. The dimensionless film volume per unit length $\rho(s, t)$ is chosen to ensure exact mass conservation as follows:

$$\rho(s,t) = \left[\cos(\beta(s)) + \frac{\mathrm{d}\beta}{\mathrm{d}s}(s)\frac{h(s,t)}{2}\right]h(s,t). \tag{9}$$

In terms of the (x, y)-coordinates of the free surface,

$$x(s,t) = s\ \sin\ \alpha - h(s,t)\cos[\alpha + \beta(s)], \tag{10a}$$

$$y(s,t) = s\ \cos\ \alpha + h(s,t)\sin[\alpha + \beta(s)], \tag{10b}$$

the exact curvature of the free surface is

$$k(s,t) = \frac{y_{ss}x_s - x_{ss}y_s}{\left[x_s^2 + y_s^2\right]^{3/2}}. \tag{11}$$

Since thin-film scalings are inappropriate in the corner puddle, isotropic spatial scalings have been used in writing (7); thus, time is scaled on $\mu H_\infty/(\varepsilon\sigma)$ (where H_∞/ε is comparable to the width of the puddle). In terms of the thin-film timescale, (7) transforms to $\rho_t + \frac{1}{3}\varepsilon^{-3}(h^3k_s)_s = 0$. At very early times, before the flow near the corner has relaxed to a quasi-static shape, we do not expect $\varepsilon^{-3}(h^3k_s)_s$ to provide an accurate representation of capillary-driven fluxes. However the free surface in the corner (where the isotropic spatial scalings are appropriate) rapidly adjusts to a quasi-static shape, and the governing equations then provide an approximation that is uniformly valid in s (albeit one that is not uniformly valid in time).

2.2. Numerical method

The evolution equations (2) and (7) were discretised in space using second-order accurate centred finite-difference approximations. Film heights and curvatures were computed on one set of $(N + 1)$ nodes, while fluxes were computed on an interlaced set. Boundary conditions were enforced using 'ghost' nodes. For all of the simulations discussed in this paper, $N = 10^4$ and MATLAB's ode15s routine with adaptive time-stepping and backward differencing was used to advance the resulting system of ODEs forward in time. The accuracy of the results was checked by independently varying the number of grid points and the domain length, by verifying numerical mass conservation to better than 0·01% and by making comparison with the asymptotic solutions described in Section 4. Finally, it was confirmed that the fluid near the far boundary remained undisturbed for the duration of each simulation.

2.2.1. *Hump*

We numerically integrated (2–4) setting the hump-width parameter $d = 0{\cdot}5$. Computations were carried out for up to $O(10^7)$ time units. We show simulations below for which $g_0 = 10$ with $L = 500$, and $g_0 = 2{\cdot}827$ and $g_0 = 4$ with $L = 5000$. To simultaneously resolve flow structures on top of the hump, near its base and in the far field, the following mapping [21, Appendix A.4] was used:

$$X = \frac{(b+1)x}{2(a+x)}, \quad \text{where } a = \frac{\bar{x}L}{L-2\bar{x}}, \quad b = \frac{a}{\bar{x}} \quad \text{and } 0 \le X \le 1. \tag{12}$$

This mapping concentrates half of the grid points (which are equispaced in X) between 0 and $\bar{x}$. We set $\bar{x} = 5$, yielding an x-grid spacing of $O(10^{-4})$ on top of the hump, $O(10^{-3})$ at its base and $O(1)$ in the far field. Validation was achieved by comparing with simulations employing an equispaced x-grid and by confirming that the numerical results were insensitive to the precise choice of $\bar{x}$. Results from these simulations are presented in Sections 3.1 and 3.3 below.

2.2.2. *Interior corner*

Numerical integrations of (7) were carried out for an interior corner semi-angle $\alpha = \pi/5$ and a domain length $L = 30$. The spine parameters B and Δ were set to $1{\cdot}5$ and $0{\cdot}02$ respectively, after ensuring that the computational results were insensitive to variations about these values. Symmetry boundary conditions were imposed at both ends of the domain:

$$y_s(0,t) = k_s(0,t) = h_s(L,t) = k_s(L,t) = 0. \tag{13}$$

For the simulations presented here, the initial puddle height $h_0 = 1{\cdot}5$. The initial free-surface distribution above the corner was chosen to be an arc of a circle of radius 2, while for $s > s_c \equiv 2\cot\alpha$, the initial film thickness was prescribed to be uniform and equal to its value at $s_c (\approx 0{\cdot}059)$. An equispaced s-grid was found to be adequate for these parameter values. Results of these simulations are shown in Section 3.2 below.

3. Numerical results

We present results here for a large hump (Section 3.1), an interior corner (Section 3.2) and small humps (Section 3.3). The meaning of the terms 'large' and 'small' will be made more precise below.

3.1. Large hump

Figure 4 shows the initial evolution of the interface and liquid pressure on top of the hump (panels a, c) and in the far field (b, d). The maximum hump height in this example is 10 times the far-field film thickness. The corresponding evolution over later times is shown in Figure 5. A local minimum in h forms at the edge of a small quasi-static drop on top of the hump; across this minimum (near $x = 0{\cdot}3$) the pressure varies sharply. The evolution of liquid on top of a hump in a bounded domain has been described in detail elsewhere [11, 12]. Under certain circumstances, up to three intermediate scaling regimes can be identified. First, the effective contact line at the edge of the drop advances slowly (like $(t/\log t)^{1/7}$). Second, the contact line is stationary and the pressure difference across the contact line drives an $O(t^{-5/4})$ flux of liquid out of the drop. Finally, the local curvature gradient drives liquid with an $O(t^{-3/2})$

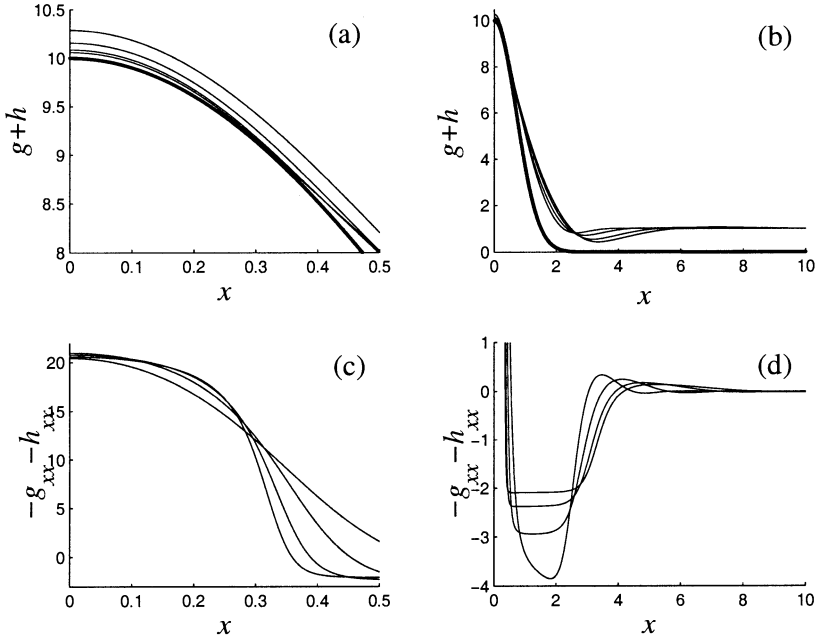

Figure 4. Thin-film flow off a large hump satisfying (2–4) with $g_0 = 10$: interface shape (a,b) and pressure (c,d) are plotted for $t = 0{\cdot}1,\ 0{\cdot}4,\ 1{\cdot}9,\ 5{\cdot}0$. The thick lines in (a, b) show the hump shape.

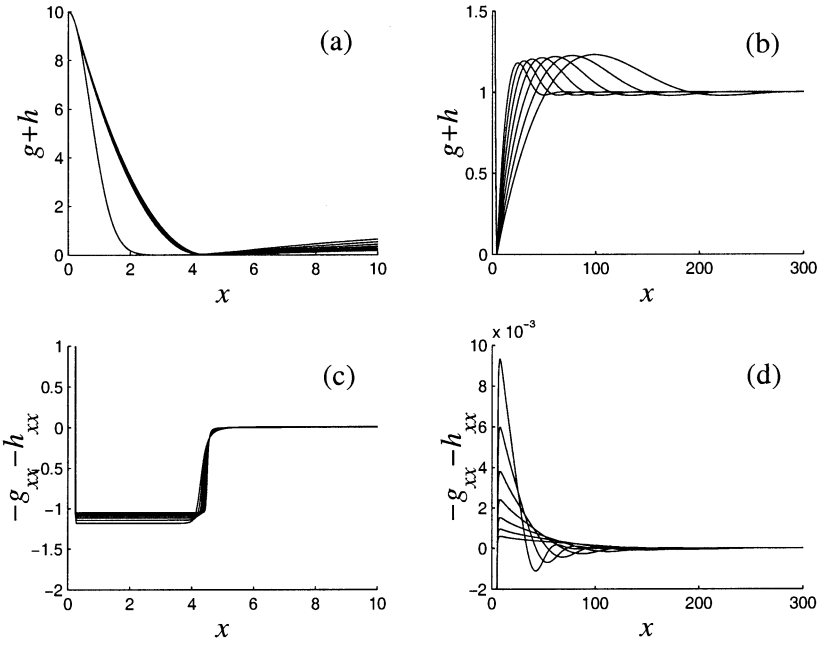

Figure 5. Thin-film flow off a large hump: interface shape (a, b) and pressure (c, d) at times $7080 \leq t \leq 3{\cdot}55\times10^6$. (a, c) show near-field and (b, d) far-field evolution. The hump is shown in (a).

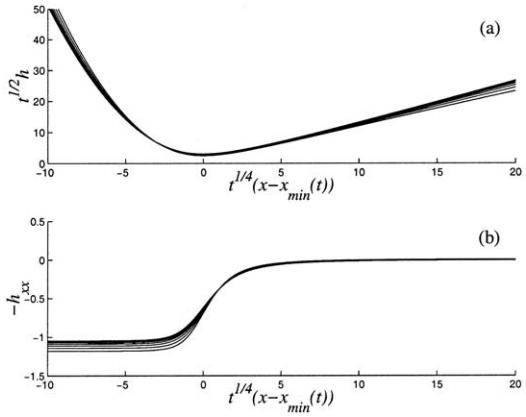

Figure 6. Thin-film flow off a large hump: the flow near the puddle's effective contact line, in rescaled variables for $7080 \leq t \leq 3{\cdot}55 \times 10^6$, showing the interface shape (a) and pressure (b).

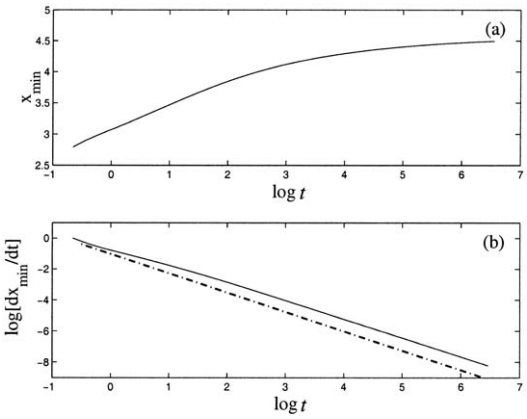

Figure 7. Location of the puddle's effective contact line $x_{\min}(t)$ (a) and its time derivative (b). The dashed line in (b) has slope $-\frac{5}{4}$.

flux out of the drop. While we ensure our numerical grid is always fine enough to resolve the corresponding flow structures, our interest here is in the behaviour elsewhere in the flow domain, so we do not describe these structures in detail below.

Figures 4 and 5 show clearly how the film evolves rapidly to form a quasi-static puddle adjacent to the hump, with its edge near $x = 4$, connected to a wave-like disturbance that propagates into the far field. We characterise the effective contact line at the edge of the puddle by the local film minimum $(x_{\min}(t), h_{\min}(t))$. At large times, $h_{\min}$ falls to zero roughly like $t^{-1/2}$, as demonstrated in Figure 6 where PDE solutions collapse when $t^{1/2}h$ and $-h_{xx}$ are plotted against $(x - x_{\min})t^{1/4}$. The local asymptotic structure resembles that identified by Jones and Wilson [19], as discussed in Section 4.1 below. $x_{\min}(t)$ evolves very slowly as t increases, approaching a finite limit as $t \to \infty$ (Figure 7a). The rate of approach is characterised in Figure 7(b), where $\mathrm{d}x_{\min}/\mathrm{d}t$ exhibits an approximate $t^{-5/4}$ scaling (justified below).

The self-similar nature of the flow in the far field is illustrated in Figure 8, which plots h and $-t^{1/2}h_{xx}$ versus $t^{-1/4}(x - x_{\min})$. The PDE data for the interface shape collapse well, showing good agreement with a similarity solution (also determined below). The pressure data (Figure 8b) also collapse well over the majority of the domain, but for x near $x_{\min}$ the rescaled pressure has a local maximum that rises slowly but indefinitely as t increases.

3.2. CORNER

Simulations for a sharp corner (obtained using (7)) show broadly similar behaviour to that for a large hump. Figure 9 shows how a quasi-static puddle forms in the corner, with a rapid jump in pressure across the effective contact line at $(s, h) = (s_{\min}(t), h_{\min}(t))$, and an unsteady wave propagating into the far field. Because the initial condition for this simulation was constructed by patching together interface shapes with piecewise uniform curvature, the relaxation of an initial jump in interfacial curvature is evident in Figure 9(c). The PDE solutions near $s_{\min}$ collapse under the same scalings used previously (Figure 10), indicating a local Jones-Wilson structure similar to that identified in Figure 6. The location of the primary local minimum $s_{\min}$ is a more complex function of time than in the previous example (Figure 11). The minimum

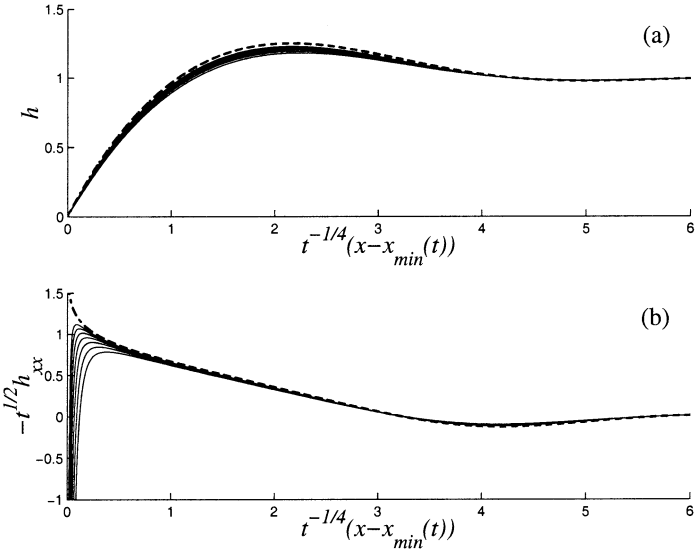

Figure 8. Far-field PDE solutions for flow off a large hump for $7080 \leq t \leq 3{\cdot}55 \times 10^6$ are plotted in rescaled variables, showing (a) film height and (b) pressure. The dashed lines show the similarity solution F_0 satisfying (20a–c).

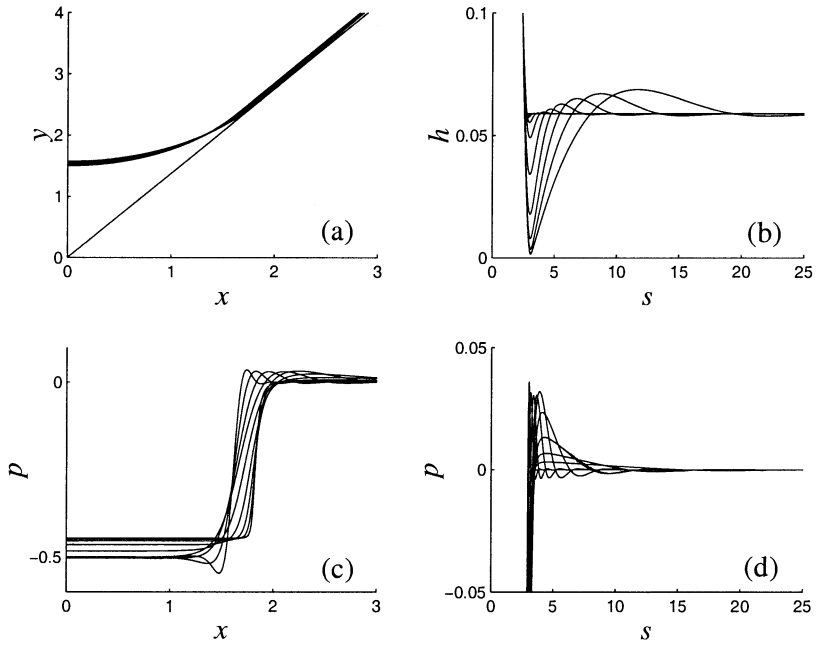

Figure 9. Flow in an interior corner: (a) the corner and interface shapes for $0{\cdot}4 \leq t \leq 10^6$ in Cartesian coordinates (10a, 10b) (the solution is symmetric about $x = 0$); (b) the far-field film evolution with respect to distance s along the wall. The near- and far-field pressure distributions are plotted with respect to x in (c) and s in (d).

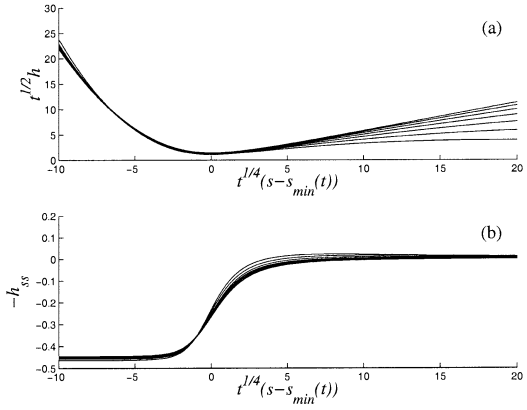

Figure 10. PDE data for flow in a corner for $3981 \leq t \leq 10^6$, rescaled and replotted showing the interface shape (a) and pressure distribution (b) near the edge of the puddle.

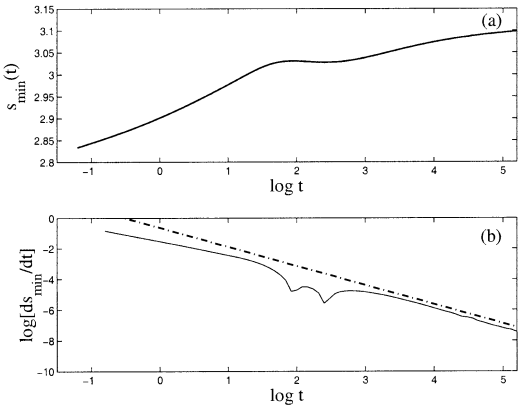

Figure 11. (a) $s_{\min}$ and (b) its time derivative as functions of time. The dashed line in (b) has slope $-5/4$.

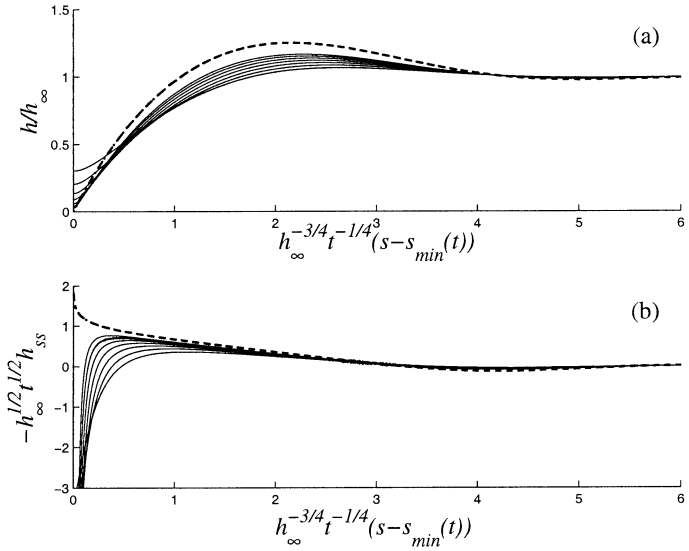

Figure 12. Thin film evolution in an interior corner: (a) the far-field interface shape (scaled on the far-field thickness h_∞) and (b) the pressure are plotted against $t^{-1/4}(s - s_{\min})$ for $3981 \leq t \leq 10^6$. The dashed lines show the similarity solution F_o satisfying (20a–c).

initially advances, reverses briefly (the change of sign in $\mathrm{d}s_{\min}/\mathrm{d}t$ leads to the kinks in the log-log graph in Figure 11b) and then advances slowly toward a finite limit. The evolution over long times again shows $\mathrm{d}s_{\min}/\mathrm{d}t$ scaling approximately like $t^{-5/4}$ at large times.

The far-field evolution of the film is also self-similar, with PDE data collapsing when the film thickness and rescaled pressure are plotted against $t^{-1/4}(s - s_{\min})$ (Figure 12). The large-time limit appears to be the same similarity solution as that shown in Figure 8 and determined below. Unlike the earlier example, there is a more noticeable drift in the maximum film height up toward the large-time limit. As before, the rescaled pressure has a local maximum for s near $s_{\min}$ that increases slowly with t.

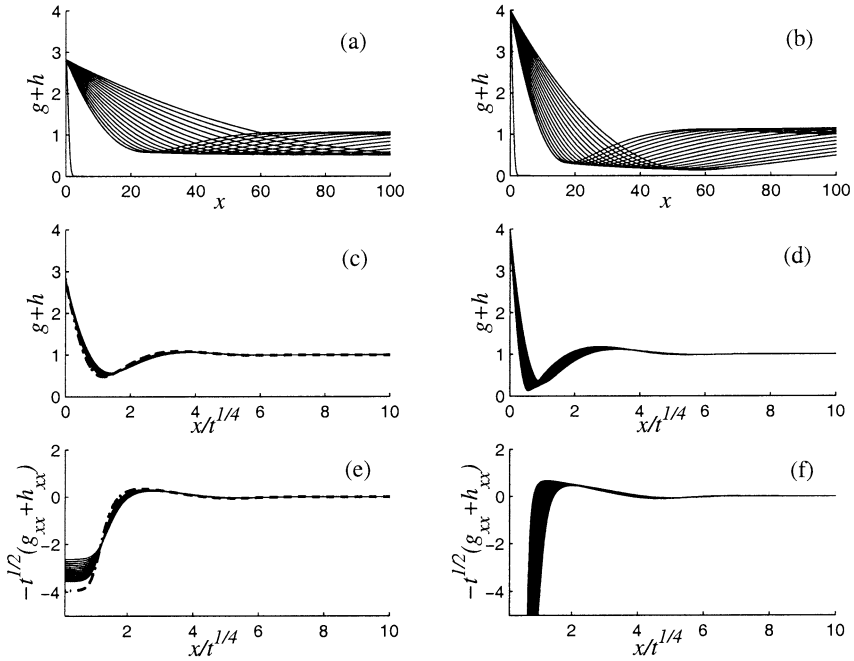

Figure 13. Flow off a hump with (a,c,e) $g_0 = 2{\cdot}827$ and (b,d,f) $g_0 = 4$. Solutions shown for $10^6 \leq t \leq 10^8$, at times equispaced in log t. (a,b) and (c,d) show film height versus x and $x/t^{1/4}$ respectively; (e,f) shows rescaled pressure. The dashed lines in (c,e) show the similarity solution satisfying (20a,b) and (38).

These observations are discussed with respect to asymptotic results in Section 4.2 below.

3.3. SMALL HUMPS

Finally we consider the drainage of a thin film off shallower humps than those considered in Section 3.1. Figure 13(a, b) shows the film thickness plotted against x when the hump has maximum height of 2·827 and of 4·0 respectively. In the former case the minimum height $h_{\min}$ remains bounded away from zero and $x_{\min}$ moves rapidly away from the hump (Figure 13a); in the latter case $h_{\min}$ appears to diminish continually towards zero, and $x_{\min}$ advances more slowly (Figure 13b). When plotted against $x/t^{1/4}$ (Figure 13c,e), the flow in the former case is self-similar for large time, approaching a similarity solution determined in Section 4.3 below uniformly. The stronger drift in the latter case (Figure 13d,f) shows that $x_{\min}$ does not scale like $t^{1/4}$, nor does it appear to be approaching a limit (as in Figure 7) over the times shown. Other simulations (not shown) indicate that the example shown in Figure 13(a,c,e) is representative of flows off humps with maximum heights less than around 3, for which $h_{\min}$ remains bounded away from zero as $t \to \infty$; comparison with flows off larger humps suggests that the example in Figure 13(b,d,e) would ultimately demonstrate pinch-off behaviour of the sort described in Section 3.1 (for which $h_{\min} \to 0$ as $t \to \infty$). Our computations therefore indicate that a qualitative transition in behaviour occurs for hump heights in the neighbourhood of 3, although in some cases it is not possible to distinguish whether or not pinch-off will ultimately occur, given the finite times available in a computation. However asymptotic analysis below predicts that the critical hump height for the transition between small- and large-hump behaviour is approximately 3·36.

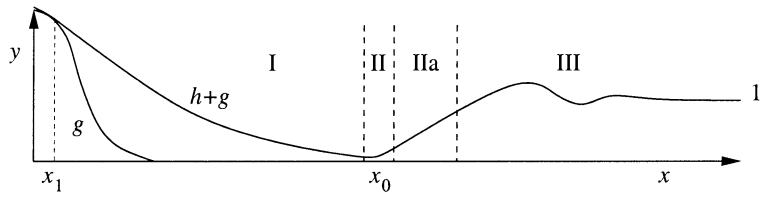

Figure 14. Schematic diagram of the four asymptotic regions of a thin film flowing off a large hump at large times.

4. Large-time asymptotics

Numerical solutions for flow off a large hump or in a sharp corner show that $h_{\min}$ tends to zero roughly like $t^{-\frac{1}{2}}$ (Figures 6, 10), while the leading edge of the disturbance in region III advances like $t^{\frac{1}{4}}$ (Figures 8, 12). We now seek the large-time asymptotic structure of these solutions. We describe the situation first for a large hump (Section 4.1, for which the local minimum at the edge of the puddle $h_{\min} \to 0$ as $t \to \infty$), then for a sharp corner (Section 4.2) and a small hump (Section 4.3, for which $h_{\min}$ remains bounded away from zero as $t \to \infty$).

4.1. LARGE HUMPS

For the case of a large hump (Figure 14) we divide the solution domain into four regions: a quasi-static slowly growing puddle (region I); a short quasi-steady region acting like a valve (II); a long region including an unsteadily propagating capillary wave (III) and a passive transitional region (IIa). We now discuss the leading-order solutions in each region.

4.1.1. *Region I*

As shown in Figure 5(c), the interface in region I has approximately uniform curvature κ and it meets the solid surfaces at its effective contact lines with zero contact angle. Let the effective contact line at $x = x_1(t)$, say, lie on the hump and that at $x = x_0(t)$, say, lie near $x_{\min}(t)$. Then the quasi-static puddle has the leading-order shape

$$h + g = \frac{1}{2}\kappa(x - x_0)^2 \qquad (x_1 \le x \le x_0), \tag{14}$$

with contact line conditions

$$g(x_1) = \frac{1}{2}\kappa(x_1 - x_0), \qquad \frac{\mathrm{d}g}{\mathrm{d}x}(x_1) = \kappa(x_1 - x_0)^2 \tag{15}$$

allowing x_1 and κ to be determined in terms of x_0 and the hump profile $g(x)$. The volume of liquid in the puddle is

$$V_I(x_0) = \int_{x_1}^{x_0} \left[\frac{1}{2}\kappa(x_0 - x)^2 - g(x)\right] \mathrm{d}x. \tag{16}$$

In certain cases x_0 is large enough relative to the width of the hump for x_1 to lie very close to the origin, in which case we may approximate the shape of the hump (3) using the expansion $g(x) = g_0 - \frac{1}{2}g_2x^2 + O(x^4)$ for given constants $g_0 > 0, g_2 > 0$. Equation (15) gives

$$\kappa = 2g_0/x_0^2 \ldots, \quad x_1 = 2g_0/(g_2x_0) + \ldots \quad \text{for} \quad g_0/(g_2x_0^2) \ll 1. \tag{17}$$

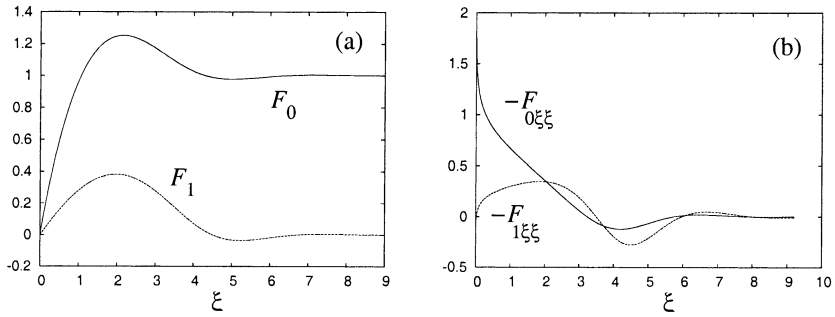

Figure 15. (a) F_0 (solid) and F_1 (dashed) versus ξ; (b) $-F_{0\xi\xi}$ (solid) and $-F_{1\xi\xi}$ (dashed) versus ξ.

In this case, with relative error $O(1/x_0)$,

$$V_I \approx \frac{1}{3} g_0 x_0 - G + \ldots \tag{18}$$

where $G = \int_0^\infty g \, \mathrm{d}x = O(1)$, assuming that $g \to 0$ sufficiently fast that $g = 0$ for $x \geq x_0$.

4.1.2. *Region III*

To capture the propagating wave (Figure 8), we seek a large-time solution of (1) of the form

$$h(x,t) = F_0(\xi) + t^{-\frac{1}{4}} M F_1(\xi) + \ldots, \qquad x = x_0(t) + \xi t^{\frac{1}{4}}, \tag{19}$$

assuming F_0, F_1 and ξ are $O(1)$. M is a constant, discussed below. We assume that $x_{0t} = O(t^{-\frac{5}{4}})$ (as indicated in Figure 7, and to be verified *a posteriori*): the slow drift of $x_0(t)$ then appears at higher orders than we consider here. We obtain at leading order from (1)

$$-\frac{1}{4}\xi F_{0\xi} + \frac{1}{3}(F_0^3 F_{0\xi\xi\xi})_\xi = 0, \tag{20a}$$

which must be solved subject to

$$F_0 \to 1 \quad \text{as} \quad \xi \to \infty, \tag{20b}$$

$$F_0 \to 0, \quad F_0^3 F_{0\xi\xi\xi} \to 0 \quad \text{as} \quad \xi \to 0. \tag{20c}$$

Linearization of F_0 around its far-field value and use of a WKB approximation shows that $F_0 \sim 1 + G_0$ where $G_0 \to 0$ as $\xi \to \infty$ and

$$G_{0\xi} \sim a \, \cos\left(\left(\frac{3}{4}\right)^{11/6} \xi^{4/3} + b\right) \exp\left(-\frac{1}{2}\left(\frac{3}{4}\xi\right)^{4/3}\right) \tag{21}$$

as $\xi \to \infty$, where a and b are constants. Here we have discarded a growing eigenmode (of the form $\exp\left[(\frac{3}{4}\xi)^{4/3}\right]$), and a further contribution that is uniform as $\xi \to \infty$. The boundary-value problem (20) therefore requires two boundary conditions to be imposed at either end of the domain.

The behaviour of F_0 as $\xi \to 0+$ takes the form

$$F_0 \sim \mathcal{A}\xi + \frac{3}{16\mathcal{A}^2}\xi^2 \log \xi + \mathcal{B}\xi^2 \tag{22}$$

for constants $\mathcal{A}$ and $\mathcal{B}$. Bowen [22] and Aradian *et al.* [18] have computed solutions of (20); for fixed $\mathcal{A}$, one can shoot for various $\mathcal{B}$ until $F_{0\xi} \to 0$ as $\xi \to \infty$ (thereby suppressing the growing eigenmode), and then rescale F_0 and ξ to satisfy (20b). As shown previously [18, 22], to satisfy (20), $\mathcal{A} \approx 1{\cdot}48$ and $\mathcal{B} \approx -0{\cdot}337$. Our approximate numerical estimates of F_0 and $-F_{0\xi\xi}$ are plotted in Figure 15; the maximum value of F_0 is close to 1·25. The pressure is weakly (logarithmically) singular as $\xi \to 0$. The leading-order flux near $\xi = 0$ is of the form $\frac{1}{3}F_0^3 F_{0\xi\xi\xi} \approx \mathcal{A}\xi^2/8$, so this solution does not account for the smaller oppositely-directed flux passing upstream through region II into region I.

Figure 8 shows how the interfacial shape computed from (2) converges to the similarity solution (20) at large times (we assume x_0 and $x_{\min}$ are sufficiently close for $(x - x_{\min})t^{-1/4}$ to be equivalent to ξ), although the pressure distribution exhibits a boundary-layer structure where $h \to 0$; we investigate this further below.

At the following order (see (19)), (1) implies that the fixed-mass correction term F_1 satisfies

$$-\frac{1}{4}F_1 - \frac{1}{4}\xi F_{1\xi} + \frac{1}{3}(F_0^3 F_{1\xi\xi\xi} + 3F_0^2 F_1 F_{0\xi\xi\xi})_\xi = 0. \tag{23}$$

Because $F_1 \to 0$ as $\xi \to \infty$, this may be integrated to give

$$-\frac{1}{4}\xi F_1 + \frac{1}{3}F_0^3 F_{1\xi\xi\xi} + F_0^2 F_1 F_{0\xi\xi\xi} = 0. \tag{24}$$

For $\xi \to \infty$, F_1 behaves like $G_{0\xi}$ in (21) (with two free parameters) implying that near $\xi = 0$, F_1 contains a free parameter that can be varied in a shooting procedure to suppress the mode that grows as $\xi \to \infty$. Because (23) is linear, we are also at liberty to normalise F_1 by imposing $\int_0^\infty F_1 \, \mathrm{d}\xi = 1$, so that F_1 describes the redistribution of a constant fluid mass M (see (19)). As $\xi \to 0$, we have

$$F_1 \sim \mathcal{D}\left[\xi + \mathcal{E}\xi^2 - \frac{\xi^2 \log \xi}{16\mathcal{A}^3} + \ldots\right]. \tag{25}$$

Our computations indicate that $\mathcal{D} \approx 0{\cdot}334$ and $\mathcal{E} \approx -0{\cdot}142$. Approximations to F_1 and $F_{1\xi\xi}$ are shown in Figure 15.

The volume of liquid in region III is $V_{\mathrm{III}} = \int_{x_0}^{L} h \, \mathrm{d}x$, where the domain length L is assumed to be large enough that $h \to 1$ well before x reaches L for all times of interest. Integration by parts allows the F_0 contribution to the integral to be evaluated exactly, because (using (20a))

$$\int_0^X F_0 \, \mathrm{d}\xi \sim X \quad \text{as} \quad X \to \infty, \tag{26}$$

so that

$$V_{\mathrm{III}} = t^{\frac{1}{4}} \int_0^{(L-x_0)/t^{\frac{1}{4}}} F_0 \, \mathrm{d}\xi + M \int_0^\infty F_1 \mathrm{d}\xi = L - x_0 + M. \tag{27}$$

The fixed mass M of fluid is therefore effectively trapped at large times by the effective contact line at $x = x_0$.

The PDE data in Figure 8 approach the similarity solution F_0 from below, so we can infer that in this example $M < 0$. Because F_1 has a maximum value near that of F_0 (Figure 15), the ξ-location of the maximum in the PDE data does not drift appreciably in Figure 8.

4.1.3. *Region II*

Motivated by the collapse of the PDE data shown in Figure 6, showing the thin self-similar draining region near the effective contact line, we follow [19, 23] and set

$$h \sim t^{-\frac{1}{2}} H(\eta), \quad x = x_0(t) + t^{-\frac{1}{4}}\eta, \tag{28}$$

where H and η are $O(1)$, so that (1) becomes $(H^3 H_{\eta\eta\eta})_\eta = O(t^{-1/2})$ (again assuming $x_{0t} = O(t^{-5/4})$). Integrating, we have $H^3_{\eta\eta\eta} = -Q$ for some constant flux $Q > 0$. Matching with region III, we require from (22) that $H_\eta \to \mathcal{A}$ as $\eta \to \infty$. To match with region I via (14), we require that $H \sim \frac{1}{2}\kappa\eta^2$ as $\eta \to -\infty$. Rescaling using $\eta = -(Q/\mathcal{A}^4)\hat{\eta}$, $H(\eta) = (Q/\mathcal{A}^3)\hat{H}(\hat{\eta})$, we obtain

$$\hat{H}^3 \hat{H}_{\hat{\eta}\hat{\eta}\hat{\eta}} = 1, \tag{29a}$$

$$\hat{H} \sim -\hat{\eta} \quad \text{as} \quad \hat{\eta} \to -\infty, \tag{29b}$$

$$\hat{H} \sim \frac{1}{2}\mathcal{C}\hat{\eta}^2 + O(1) \quad \text{as} \quad \hat{\eta} \to \infty, \tag{29c}$$

where $\mathcal{C} = \kappa Q/\mathcal{A}^5$. We have suppressed the linear term in (29c) via a transverse displacement in η; x_0 and $x_{\min}$ are thus separated at large times by an $O(t^{-1/4})$ distance. Equation (29) has a unique solution, with $\mathcal{C} \approx 1{\cdot}2098$ and $\hat{H}_{\min} \equiv \mathcal{H} \approx 1{\cdot}2593$ [10, 23, 24], resembling the collapsed curves in Figure 6. This determines Q in terms of $\kappa(x_0)$.

4.1.4. *Region IIa*

While we have matched the interfacial slopes between regions II and III, the fluxes and pressures do not yet match: the flux $\frac{1}{3}h^3 h_{xxx}$ through region II is $-\frac{1}{3}Qt^{-5/4}$, for example, while that entering region III is $\mathcal{A}(x - x_0)^2/8t^{5/4}$. It is therefore necessary to introduce a further region across which h is approximately linear but the flux varies, accounting for the boundary-layer behaviour in the pressure seen in Figure 8. We therefore set

$$h = t^{-\frac{1}{4}}\mathcal{A}z + t^{-\frac{1}{2}}\hat{h}(z) + \ldots, \qquad x = x_0(t) + z, \tag{30}$$

assuming z and $\hat{h}$ are $O(1)$. Once again, assuming $x_{0t} = O(t^{-5/4})$ allows us to neglect contact-line drift in what follows. Substituting in (1) gives

$$-\frac{1}{4}\mathcal{A}z + \frac{1}{3}\mathcal{A}^3\left(z^3\hat{h}_{zzz}\right)_z = 0. \tag{31}$$

Integrating, we obtain

$$h = \frac{\mathcal{A}z}{t^{\frac{1}{4}}} + \frac{3}{\mathcal{A}^2 t^{\frac{1}{2}}}\left[\frac{1}{16}z^2\,\log z + az^2 + bz + c\,\log z + d\right] + \ldots \tag{32}$$

for constants a, b, c and d. The outer limit (29b) of region II can be written $H \sim A\eta - \frac{1}{2}Q\mathcal{A}^{-3}\log\eta + O(1)$, while the leading-order inner limit of III is given by (22) plus a correction from (25). Matching allows us to write (32) as

$$h = \frac{\mathcal{A}z}{t^{\frac{1}{4}}} + \frac{1}{t^{\frac{1}{2}}}\left[\frac{3}{16\mathcal{A}^2}z^2\log z + \left(\mathcal{B} - \frac{3}{16\mathcal{A}^2}\log(t^{\frac{1}{4}})\right)z^2 + M\mathcal{D}z - \frac{Q}{2\mathcal{A}^3}\log z + O(1)\right] + \ldots,$$

(where for brevity we here treat $\log(t)$ as an $O(1)$ quantity). Differentiating, we then find the flux in this region to be

$$\frac{1}{3}h^3h_{zzz} = t^{-\frac{5}{4}}\left[\frac{1}{8}\mathcal{A}z^2 - \frac{1}{3}Q\right]. \tag{33}$$

Thus region IIa acts as a buffer, providing a source of liquid that can flow both downstream to region III (in $z > (8Q/3\mathcal{A})^{\frac{1}{2}}$) and upstream into region I (from $z < (8Q/3\mathcal{A})^{\frac{1}{2}}$). The pressure

$$p = -h_{zz} \sim -\frac{1}{t^{\frac{1}{2}}}\left[\frac{3}{16\mathcal{A}^2}\left(3 + 2\log\left(\frac{z}{t^{1/4}}\right)\right) + 2\mathcal{B} + \frac{Q}{2\mathcal{A}^3z^2}\right] \tag{34}$$

has a maximum value $p_{\max} \approx 3\log t/(32\mathcal{A}^2t^{\frac{1}{2}})$. This time-dependence explains the slow rise in the maximum pressure near the origin seen in Figure 8.

4.1.5. *Mass conservation*

Fluid volume must be conserved during the evolution of the film. Because $h(x, 0) = 1$ in $0 < x < L$, for $t \gg 1$ the total fluid volume $V = L$, where $V \approx V_{\mathrm{I}} + V_{\mathrm{III}}$ (neglecting the asymptotically negligible volume in region II). Thus, from (16) and (27),

$$x_0 \sim V_{\mathrm{I}}(x_0) + M, \tag{35}$$

where M is the mass of fluid trapped in (or lost from) region III. Equation (35) shows that the length of region I is determined (through M) by the dynamics over intermediate timescales. Once t is large, and the film pinches off to form an effective contact line, there is minimal fluid exchange between regions I and III. We cannot predict the size (or even sign) of M from the large-time asymptotic analysis. However, we can check the consistency of (35). At large times, $x_0 \approx 4{\cdot}51$ (Figure 7) and hence $V_I(x_0) \approx 6{\cdot}91$ from (16); (35) implies $M < 0$, as already observed from Figure 8.

Because h remains non-zero in region II there is still a weak flux of liquid drawn into region I from region IIa. The puddle in region I grows continually and x_0 advances slowly, with $V_{\mathrm{I}}'(x_0)x_{0t} = \frac{1}{3}Qt^{-\frac{5}{4}}$. Assuming $x_0 \to x_{00}$, say, as $t \to \infty$, we may therefore write

$$x_0(t) \sim x_{00} - \frac{4\mathcal{A}^5\mathcal{C}}{3\kappa(x_{00}V_{\mathrm{I}}'(x_{00}))t^{\frac{1}{4}}}, \tag{36}$$

where the contact line's ultimate equilibrium location x_0 satisfies $x_{00} = V_{\mathrm{I}}(x_{00}) + M$. Thus $x_{0t} = O(t^{-5/4})$, which is small enough to ensure neglect of the contact-line drift terms in the analysis above, and in agreement with Figure 7.

In the special case when x_1 lies near the origin and x_0 is large, we have from (18) $x_0 \approx (G - M)/(\frac{1}{3}g_0 - 1)$. This approximation therefore requires that $g_0 \to 3+$ to ensure that $x_0 \gg 1$. However, Figure 13 indicates that alternative behaviour arises once g_0 is as small as 3: we investigate this in Section 4.3 below.

4.2. CORNERS

Having established the large-time asymptotic structure for flow off a large hump, we can also apply it to flow in a sharp corner. The collapsed PDE data shown in Figure 10 near the pinch-off point again reveal the familiar Jones-Wilson region-II structure satisfying (29). Figure 12 shows how the collapsed data downstream of the pinch-off point approach the region-III similarity solution (20) at large times. However the PDE data lie further from F_0 than in the case for a hump (Figure 8), indicating that for the corner simulation the mass deficit M

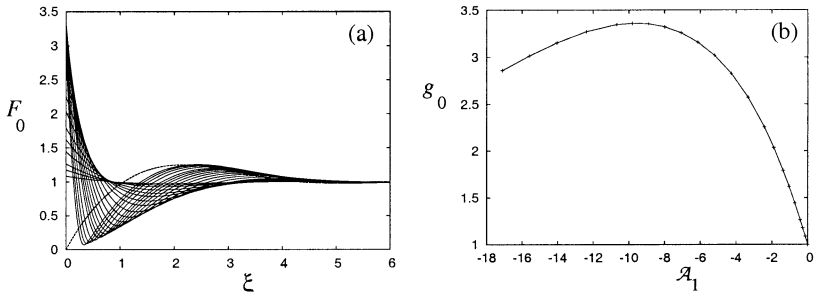

Figure 16. (a) Solid curves show $F_0(\xi)$ satisfying (20a,b), (38) for values of $\mathcal{A}_1$ shown with dots in (b); the dotted line shows the solution of (20); (b) g_0 versus $\mathcal{A}_1$.

is larger. (This is presumably because our simulations used a non-uniform initial condition that distributed additional mass near the vertex of the corner). Since $F_1 = 0$ near $\xi = 4{\cdot}50$ (Figure 15a), we expect the PDE data and F_0 to be in close agreement here: they intersect in Figure 12 just beyond $\xi = 4$. Finally, the slow drift of the puddle's effective contact line shown in Figure 11 has a time-dependence consistent with (36).

Once again, the large-time asymptotic analysis tells us that transient dynamics determine the mass of fluid partitioned between the puddle and the far field by pinch-off, and hence the ultimate size of the puddle in the corner.

4.3. SMALL HUMPS

Figure 13 suggests that for small Gaussian humps (with g_0 between 1 and approximately 3) at large times, a similarity solution of the form outlined for region III above attaches close to the top of the hump. To describe this case, we set

$$h(x,t) = F_0(\xi) + Mt^{-\frac{1}{4}}F_1(\xi) + \ldots, \quad x = \xi t^{\frac{1}{4}}, \tag{37}$$

assuming F_0, F_1 and ξ are $O(1)$ and $\int_0^\infty F_1 \, \mathrm{d}\xi = 1$. At leading order F_0 satisfies (20a,b) plus

$$F_0 = g_0, \qquad F_{0\xi\xi\xi} = 0 \quad \text{at} \quad \xi = 0. \tag{38}$$

We justify these boundary conditions by considering an inner region where $x = O(1)$ in the neighbourhood of the hump, where the flow satisfies (2). Assuming the flow is locally quasi-steady, we have $Q = \frac{1}{3}h^3(h + g_{xxx}$ in this region, for same constant Q. To satisfy the no-flux condition at the origin we require $Q = 0$. Thus $h + g = Ax^2 + Bx + C$ for some constants A, B, C. To match with the outer similarity solution (37) (where $g \to 0$) we require $A = B = 0$. We then impose zero contact angle at some point $x = x_1$ on the hump, so that $h(x_1) = 0$ and $h_x(x_1) = 0$. Since $h_x(x_1) + g_x(x_1) = 0$ to leading order, $g_x(x_1) = 0$ and hence $x_1 = 0$. Then $h(0) = 0$ requires $C = g_0$, yielding (38) as leading-order boundary conditions for the outer flow.

The local solution of (20a,b; 38) near $\xi = 0$ has two free parameters, $F_0 \sim g_0 + \mathcal{A}_1\xi + \mathcal{A}_2\xi^2 + O(\xi^4)$. Solutions can be obtained by fixing g_0 and $\mathcal{A}_1$, shooting with varying $\mathcal{A}_2$ to suppress the growing mode for large ξ, and then rescaling ξ and F_0 to enforce (20b), thus changing the value of g_0. This yields a one-parameter family of similarity solutions. Numerical approximations to members of this family are shown in Figure 16. It is convenient to parameterize solutions numerically using $\mathcal{A}_1 < 0$. As $\mathcal{A}_1$ falls from zero, solutions increase in amplitude until $\mathcal{A}_1 = \mathcal{A}_c \approx -9{\cdot}8$ when g_0 takes a maximum value $g_c \approx 3{\cdot}36$. As $\mathcal{A}_1$

becomes increasingly negative, the solutions appear to approach the solution satisfying (20) as $\mathcal{A}_1 \to -\infty$ (see Figure 16; we did not attempt to compute solutions for $\mathcal{A}_1 < -17{\cdot}11$). Parameterizing solutions using g_0, computations therefore indicate that (20a, b; 38) has two solution branches for $1 < g_0 < g_c$, and no solutions for $g_0 > g_c$.

Figure 13 demonstrates how PDE data for $g_0 = 2{\cdot}827$ converge to the corresponding similarity solution satisfying (20a,b; 38). We therefore conjecture that the branch of solutions in Figure 16(b) between $\mathcal{A}_c < \mathcal{A}_1 < 0$ is stable, while the branch in $\mathcal{A}_1 < \mathcal{A}_c$ is unstable.

For a given g_0, assuming a solution exists, we can define

$$M(g_0) = -\int_0^\infty (F_0 - 1)\, \mathrm{d}\xi. \tag{39}$$

At the following order, as before, (23) may be integrated to give (24). The local behaviour near $\xi = 0$ also contains two parameters, one to suppress the growing far-field eigenmode and one to normalise F_1 so that it has unit integral. Thus $F_1 \sim \mathcal{D}_1[\xi + \mathcal{D}_2\xi^2 + O(\xi^5)]$, where $\mathcal{D}_1(g_0)$ and $\mathcal{D}_2(g_0)$ can be determined numerically. The formulation in (37) ensures volume conservation: the mass excess or deficit in F_0 distributes itself through the F_1 term. In contrast to the large hump case, we can predict *M a priori* using (39).

5. Discussion

We have shown, through numerical solution of evolution equations and supporting large-time asymptotics, that a spatially unbounded thin film coating a sufficiently large hump readjusts to form a quasi-static puddle bounded by an effective contact line at which the local minimum film thickness $h_{\min} \to 0$ as $t \to \infty$. As time increases, the contact line drifts slowly towards a limiting position. This position is determined by the transient dynamics: as the film pinches off, it traps a certain volume of fluid in the puddle and this volume dictates the contact-line's ultimate location. Using an evolution equation based on lubrication theory but accounting accurately for mass conservation and interfacial curvature, we found that thin-film flow in a sharp corner exhibits broadly similar features. This suggests that similar behaviour can also be expected when liquid bridges form between touching wet surfaces.

In practice, numerous physical effects that we have neglected here may be important. We have allowed the film to readjust through the formation of a capillary wave that propagates off into the far field. In any practical situation, the wave will reach a boundary, so that at sufficiently large times the effect of a far-field no-flux boundary condition (for example) will be felt by the film ahead of the contact line. At very large times the puddle is likely to adjust slowly to new configurations dependent on the total volume of fluid in the domain. The solutions we present here therefore have value as intermediate asymptotics. Further effects that are likely to be significant in practical applications include disjoining forces causing the film to rupture once it thins sufficiently, surfactant causing interfacial immobilisation and further changes in the shape or length of the underlying substrate.

For shallow humps, a qualitatively different flow structure emerges. We calculated members of the family of similarity solutions describing an unsteadily propagating capillary wave that connects directly onto the top of the hump at large times. This family has a turning point when parameterized by the hump height (Figure 16), so that no solutions exist for hump heights in excess of $g_c \approx 3{\cdot}36$ times the far-field film thickness. Our simulations support the conjecture that one branch of similarity solutions is stable, the other is unstable, as illustrated schematically in Figure 17. (We did not explicity test the stability of the unstable

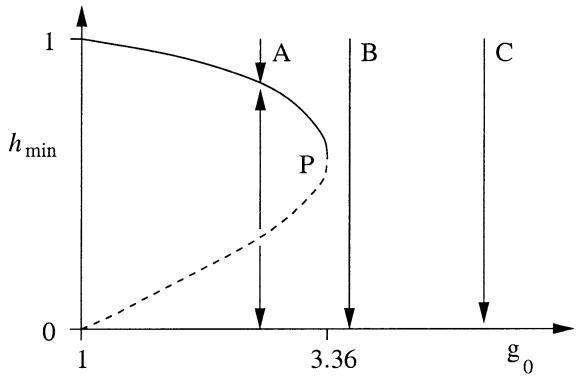

Figure 17. A conjectured schematic bifurcation diagram indicating the evolution of flow off humps with different maximum heights. For $g_0 < 3{\cdot}36$ (case A), the initially uniform state approaches a similarity solution at large times for which local minimum at the edge of the puddle $h_{\min}$ is bounded away from zero; for $g_0 > 3{\cdot}36$, $h_{\min} \to 0$ as $t \to \infty$. In case B the evolution is likely to be slow in the neighbourhood of the turning point P; the evolution is more rapid in case C.

branch by integrating numerically using suitable initial conditions.) On the stable branch, the local minimum in film depth at the edge of the quasi-static puddle adjacent to the hump is bounded away from zero, and the minimum advances away from the hump approximately like $t^{1/4}$. Because $h_{\min}$ does not approach zero, mass is not trapped in the puddle, but instead redistributes in a way that can be determined via large-time asymptotic analysis. For hump heights in excess of 3·36, an initially uniform-thickness film ultimately pinches off, with $h_{\min} \to 0$ as $t \to \infty$. We conjecture that pinch-off may also occur for $g_0 < g_c$ provided suitable initial conditions are chosen, but we did not explore that possibility here. Simulations indicate that it may sometimes be difficult to distinguish between pinch-off and no-pinch-off behaviour experimentally, because for near-critical hump heights (*e.g.*, case B in Figure 17, or the simulation shown in Figure 13b,d,f) the distinction between such solutions emerges only at very large times. However, it should be possible to verify the predictions of this analysis for more extreme hump heights. We conjecture that similar flow structures also arise for shallow corners, although we have not investigated that limit here.

Acknowledgements

We wish to acknowledge the important contributions of Jan Rosenzweig to the early stages of this work, and financial support from the University of Nottingham and Wellcome Trust grant 061142.

References

1. J. Rosenzweig and O. E. Jensen, Capillary-elastic instabilities of liquid-lined lung airways. *J. Biomech. Engng.* 124 (2002) 650–655.
2. R. J. Braun and A. D. Fitt, Modelling drainage of the precorneal tear film after a blink. *Math. Med. Biol.* 20 (2003) 1–28.
3. T. G. Myers, Thin films with high surface tension. *SIAM Rev.* 40 (1998) 441–462.
4. A. Oron, S. H. Davis and S. G. Bankoff, Long-scale evolution of thin liquid films. *Rev. Mod. Phys.* 69 (1997) 931–980.

5. L. W. Schwartz and D. E. Weidner, Modeling of coating flows on curved surfaces. *J. Engng. Math.* 29 (1995) 91–103.
6. R. V. Roy, A. J. Roberts and M. F. Simpson, A lubrication model of coating flows over a curved substrate in space. *J. Fluid Mech.* 454 (2002) 235–261.
7. L. E. Stillwagon and R. G. Larson, Fundamentals of topographic substrate levelling. *J. Appl. Phys.* 63 (1988) 5251–5258.
8. S. Kalliadasis S. C. Bielarz and G. M. Homsy, Steady free-surface thin film flows over topography. *Phys. Fluids* 12 (2000) 1889–1898.
9. L. E. Stillwagon and R. G. Larson, Leveling of thin films over uneven substrates during spin coating. *Phys. Fluids* A2 (1990) 1937–1944.
10. O. E. Jensen, The thin liquid lining of a weakly curved cylindrical tube. *J. Fluid Mech.* 331 (1997) 373–403.
11. J. Rosenzweig, *Capillary-Elastic Instabilities and Draining Flows in Buckled Lung Airways*. Ph.D. Thesis, University of Cambridge (2000) 139pp.
12. J. Rosenzweig and O. E. Jensen, Long-time draining of thin liquid films in buckled lung airways. In: A. C. King and Y. D. Shikmurzaev (eds.), *IUTAM Symposium on Free Surface Flows*. Dordrecht: Kluwer Academic Publishers (2001) pp. 265–272.
13. P. D. Howell, Surface-tension-driven flow on a moving curved surface. *J. Engng. Math.* 45 (2003) 283–308.
14. T. G. Myers, J. P. F. Charpin and S. J. Chapman, The flow and solidification of a thin fluid film on an arbitrary three-dimensional surface. *Phys. Fluids* 14 (2002) 2788–2803.
15. M. Heil and J. P. White, Airway closure: surface-tension-driven non-axisymmetric instabilities of liquid-lined elastic rings. *J. Fluid Mech.* 462 (2002) 79–109.
16. R. Stocker and A. E. Hosoi, Lubrication in a corner. *J. Fluid Mech.* (submitted) (2004).
17. R. Stocker and A. E. Hosoi, Corner flow in free liquid films. *J. Engng Math.* 50 (2004) 267–288.
18. A. Aradian, E. Raphaël and P. G. de Gennes, 'Marginal pinching' in soap films. *Europhys. Lett.* 55 (2001) 834–840.
19. A. F. Jones and S. D. R. Wilson, The film drainage problem in droplet coalescence *J. Fluid Mech.* 87 (1978) 263–288.
20. S. F. Kistler and L. E. Scriven, Coating Flows. In: J. Pearson and S. Richardson (eds.), *Computational Analysis of Polymer Processing*. London: Applied Science Publishers (1983) pp.243–299.
21. P. J. Schmid and D. S. Henningson, *Stability and Transition in Shear Flows.* New York: Springer-Verlag (2001) 556pp.
22. M. Bowen, *High Order Diffusion*. Ph.D. Thesis, University of Nottingham (1998) 187pp.
23. P. Hammond, Nonlinear adjustment of a thin annular film of viscous fluid surrounding a thread of another within a circular cylindrical pipe. *J. Fluid Mech.* 137 (1983) 363–384.
24. H. Wong, C. J. Radke and S. Morris, Motion of long bubbles in polygonal capillaries. Part 1. *J. Fluid Mech.* 292 (1995) 71–94.